ACS OMEGA

http://pubs.acs.org/journal/acsodf

Article

Facile Synthesis of Gram-Scale Mesoporous Ag/TiO_2 Photocatalysts for Pharmaceutical Water Pollutant Removal and Green Hydrogen Generation

Yassine Cherif, Hajer Azzi,* Kishore Sridharan, Seulgi Ji, Heechae Choi, Michael G. Allan, Sihem Benaissa, Karima Saidi-Bendahou, Lois Damptey, Camila Silva Ribeiro, Satheesh Krishnamurthy, Sanjay Nagarajan, M. Mercedes Maroto-Valer, Moritz F. Kuehnel, and Sudhagar Pitchaimuthu*

Cite This: *ACS Omega* 2023, 8, 1249−1261

Read Online

ACCESS | Metrics & More | Article Recommendations | Supporting Information

ABSTRACT: This work demonstrates a two-step gram-scale synthesis of presynthesized silver (Ag) nanoparticles impregnated with mesoporous TiO_2 and evaluates their feasibility for wastewater treatment and hydrogen gas generation under natural sunlight. Paracetamol was chosen as the model pharmaceutical pollutant for evaluating photocatalytic performance. A systematic material analysis (morphology, chemical environment, optical bandgap energy) of the Ag/TiO_2 photocatalyst powder was carried out, and the influence of material properties on the performance is discussed in detail. The experimental results showed that the decoration of anatase TiO_2 nanoparticles (size between 80 and 100 nm) with 5 nm Ag nanoparticles (1 wt %) induced visible-light absorption and enhanced charge carrier separation. As a result, 0.01 g/L Ag/TiO_2 effectively removed 99% of 0.01 g/L paracetamol in 120 min and exhibited 60% higher photocatalytic removal than pristine TiO_2. Alongside paracetamol degradation, Ag/TiO_2 led to the generation of 1729 μmol H_2 g^{-1} h^{-1}. This proof-of-concept approach for tandem pollutant degradation and hydrogen generation was further evaluated with rare earth metal (lanthanum)- and nonmetal (nitrogen)-doped TiO_2, which also showed a positive response. Using a combination of *ab initio* calculations and our new theory model, we revealed that the enhanced photocatalytic performance of Ag/TiO_2 was due to the surface Fermi-level change of TiO_2 and lowered surface reaction energy barrier for water pollutant oxidation. This work opens new opportunities for exploiting tandem photocatalytic routes beyond water splitting and understanding the simultaneous reactions in metal-doped metal oxide photocatalyst systems under natural sunlight.

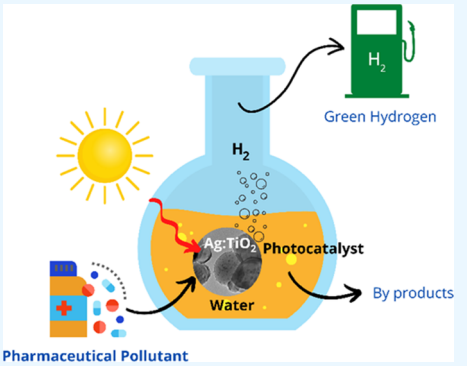

INTRODUCTION

The increasing diversity of water pollutants has led to a growing global need to protect public health and the ecosystem.[1] In particular, emerging pollutants such as pharmaceutical and personal care products (PPCPs) are a unique group of environmental contaminants due to their inherent ability to induce physiological effects in humans, even at low concentrations. These pollutants are becoming ubiquitous in the environment as they cannot be effectively removed by conventional wastewater treatment stages due to their toxicity and recalcitrance. Since these PPCPs may have adverse effects on humans and ecosystems, their eradication is of great interest in health and environmental risk management. To this end, advanced oxidation processes and especially semiconductor-based photocatalysis have recently gained increased attention to remove PPCPs due to their rapid degradation rates, cost-effectiveness, and mineralization capability.[2−4]

Under light irradiation, a valence band hole is created in a semiconductor photocatalyst alongside a photoexcited electron at the conduction band. These hole carriers lead to the formation of hydroxyl ($^{\bullet}OH^{-}$) radicals; also, the photoelectrons at the conduction band generate superoxide ($^{\bullet}O_2^{-}$) and both are capable of degrading PPCP pollutants in water. Practically, TiO_2 is the most active photocatalyst used in wastewater treatment owing to its high chemical stability, nontoxicity, high oxidation/reduction potential, and low cost.[5,6] Recent reviews and research articles have emphasized the advantages of TiO_2 photocatalyst-assisted pharmaceutical pollutant degradation.[7−9] Mesoporous TiO_2 has received much attention in photocatalytic wastewater treatment in recent times because it contains a highly interconnected pore network, which is favorable for the diffusion of reactants and

Received: October 15, 2022
Accepted: December 9, 2022
Published: December 28, 2022

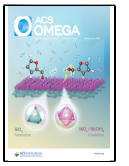

products, and a large surface area, which offers more active sites.[10−12] Owing to their excellent photocatalytic performance for pollutant oxidation[13−15] and hydrogen generation,[16−18] significant progress in synthesizing mesoporous TiO_2 has been made in recent years. However, the quantum efficiency of mesoporous TiO_2 is still not high enough (<1%) at present for practical applications. Many factors affect the photocatalytic activity of mesoporous TiO_2, such as its specific surface area, crystallinity, etc. Various synthesis methods and modifications have been proposed to improve the photocatalytic performance of mesoporous TiO_2, and their effects have been significant. Heteroatom doping effectively modifies TiO_2 by introducing additional extrinsic electronic levels in the energy bandgap, thereby promoting visible-light absorption. For instance, metal doping into TiO_2 creates intra-bandgap states due to the integration of metal dopants. Thus, the bandgap energy decreases mainly due to the lowering of the TiO_2 conduction band. On the other hand, narrowing the bandgap at the desired level by incorporating nonmetal doping ions is even better. It creates oxygen vacancies (O_v),[19] which modify the electronic properties, surface chemistry, and coordination environment at TiO_2, enhancing the visible-light activity and charge separation, thus promoting photocatalytic performance.[20,21] Recently, a series of heteroatom dopants, including metal and nonmetal atoms (e.g., Cu, Ag, Au, La, N, C, etc.), have been reported to enhance the performance of mesoporous TiO_2.[22−30] In addition, reduced graphene oxide[31,32] and graphene quantum dot (QD) composites[33,34] also promoted charge transfer at TiO_2 photocatalysts. The metal dopant dramatically increases the oxygen vacancy at the TiO_2 lattice, modifies electron density, and reduces recombination between electron−hole pairs at the photocatalyst. Among different metals, silver (Ag) has a significant advantage of nontoxicity, lower cost, and higher antibacterial properties compared to its expensive counterparts (Au and Pt).[35−38] Ag doping is commonly used to reduce the bandgap energy and minimize recombination by acting as an electron trap. Hence, Ag assists in charge separation by forming a Schottky barrier between TiO_2 and metal. It also enhances the visible-light absorption of TiO_2 due to the localized surface plasmon resonance (LSPR) originating from the oscillation of surface electrons.[39]

Recently, simultaneous pollutant degradation and hydrogen generation have received significant attention for addressing the energy demand and environmental clean-up concurrently.[40−43] This dual process in one pot is expected to reduce the operating cost of both reactions carried out individually. Currently, there is little understanding of the influence of the photocatalyst surface properties on such tandem reactions, particularly regarding photocatalysts for concurrent pharmaceutical pollutant degradation and hydrogen generation. A major issue is high charge recombination rates at the photocatalyst surface severely affecting their performance. To address these challenges, this work explores the feasibility of material modification of the TiO_2 photocatalyst in simultaneous water pollutant degradation and hydrogen generation.

The main objective of the work was to design high surface area mesoporous TiO_2 coated with Ag nanoparticles by a two-step wet chemical synthesis process. The resultant Ag/TiO_2 photocatalyst was tested for simultaneous paracetamol degradation and hydrogen gas recovery under natural sunlight. Furthermore, the tandem process was also evaluated with nonmetal (nitrogen)- and rare earth metal (Ln)-doped TiO_2 photocatalysts. The origin of the photocatalytic performance of pristine TiO_2 and Ag/TiO_2 was examined with atomic-scale modeling using *ab initio* calculations and a Fermi-level-dependent adsorption energy theory model.

EXPERIMENTAL SECTION

Chemicals. Titanium butoxide (Sigma-Aldrich, 97%), PEG-PPG-PEG P123 (Sigma-Aldrich, 97%), acetic acid (Sigma-Aldrich, 97%), absolute ethanol (Honeywell Riedel-de Haën, 99.8%), silver nitrate (Sigma-Aldrich, 99%), sodium citrate tribasic dihydrate (Fluka Analytical, 99.0%), urea (Sigma-Aldrich, 99%), and lanthanum nitrate hexahydrate (Sigma-Aldrich, 99.999%) were used for the experiments. All of the chemicals were used as it is without filtering.

Preparation of Bare and Ag-Doped Mesoporous TiO_2. Mesoporous titania was prepared by the hydrothermal-assisted sol−gel method, as described by Liu et al.,[44] with the following steps. First, *Solution A* was prepared by dropwise addition of 5 g of titanium butoxide into 30 mL of the 20% aqueous acetic acid solution under constant stirring for 4 h. Second, *Solution B* was obtained by dissolving 3 g of the block copolymer (Pluronic P123) in 20 mL of ethanol. In the third step, *Solution B* was added dropwise to *Solution A* and stirred at 150 RPM under room temperature for 24 h before crystallizing at 100 °C for 48 h in a Teflon-lined autoclave. After cooling the autoclave to room temperature, the solid product was collected by filtration, washed several times with distilled water, and dried in an oven at 80 °C overnight. Template removal was achieved by air calcination at 500 °C for 4 h with a ramping rate of 1 °C/min. The entire synthesis was carried out under standard atmospheric conditions.

Ag nanoparticle-coated mesoporous titania was synthesized by a simple chemical method developed by Naik et al.,[45] in which $AgNO_3$ is reduced by trisodium citrate. On previously prepared calcined mesoporous TiO_2, different wt % (0.5 and 1) of Ag nanoparticles were introduced via the following procedure: an aqueous solution containing an appropriate amount of $AgNO_3$ was heated at 80 °C for 20 min in a round-bottomed flask. Then, 0.5 g of mesoporous titania was added to this solution and kept under stirring (150 RPM) for 30 min. The 0.002 M trisodium citrate aqueous solution was then added dropwise to the mixture. After 1 h of stirring (150 RPM), the solution was cooled to room temperature, filtered and washed five times with 60 °C deionized water, and then dried in a vacuum oven at 60 °C for 60 h. The photographs of pure and Ag nanoparticle-coated TiO_2 powders at the gram scale are presented in Figure S1.

Preparation of N- and La-Doped Mesoporous TiO_2. The photocatalytic performance of Ag/TiO_2 was compared against other doped titania. First, nitrogen-doped mesoporous titania with N/TiO_2 molar ratio equal to 3 was prepared as reported by Jian et al.,[46] in which urea was used as the nitrogen source and mixed with TiO_2 in an agate mortar. The resulting mixture was calcined at 500 °C (10 °C/min) for 1 h. The photocatalyst is denoted as N/TiO_2 from hereon. In the case of lanthanum (La)-doped TiO_2, 2 wt % of lanthanum was impregnated on calcined mesoporous TiO_2 by the incipient wet impregnation technique using lanthanum nitrate as the La source. TiO_2 was mixed with the 0.002 M aqueous solution of lanthanum nitrate at 60 °C in a rotary evaporator. Then, the impregnated powder was dried at 100 °C overnight and calcined in air at 500 °C for 4 h (heating rate: 1 °C/min).

https://doi.org/10.1021/acsomega.2c06657
ACS Omega 2023, 8, 1249−1261

Catalyst Characterization. The X-ray diffraction (XRD) patterns were recorded using a Rigaku MiniFlex 600 diffractometer equipped with monochromatized Cu Kα radiation (λ = 15,418 Å). The morphology of the powder samples was characterized by high-resolution transmission electron microscopy (HRTEM, JEM2000EX). X-ray photoelectron spectroscopy (XPS) spectra were performed with a Kratos XSAM 800 kit having a dual anode X-ray source. The N_2 adsorption/desorption isotherms were carried out on a 3Flex instrument (Micromeritics). The specific surface areas of the samples were calculated by the BET method. The UV−vis diffuse reflectance spectra of the photocatalysts were recorded on a SPECORD 200 Plus UV−vis spectrophotometer. Raman spectra were recorded on a UV resonance Raman spectrometer (Horiba LabRAM HR Evolution Raman spectrometer). The laser excitation was at 633 nm.

Photocatalytic Paracetamol Degradation. The photocatalytic activity of pristine TiO_2 and Ag/TiO_2 was assessed by observing the degradation of paracetamol under natural solar light irradiation (latitude: 34°52′41.99″N; longitude: −1°18′54.00″W) on June 2021 from 12 to 2 pm as shown in Figure S2. The outside temperature was 28 °C, whereas the experimental solutions reached 36 °C. The reaction slurry was prepared by suspending 100 mg of the photocatalyst in 100 mL of an aqueous paracetamol solution (10 mg/L). The slurry was stirred in the dark for 30 min to ensure the adsorption of paracetamol molecules on the surface of the photocatalysts. During the photocatalytic reaction, aliquots (5 mL) of the reaction slurry were withdrawn at regular intervals of time, centrifuged (4500 RPM for 10 min) to separate the photocatalyst, and the supernatant was stored in amber glass vials. To determine the performance variability, all experiments were conducted in triplicates. The rate of the photocatalytic degradation of paracetamol was determined from the absorption spectra of the centrifuged aliquots that were measured using a UV−vis spectrophotometer (SPECORD 200 PLUS) and were compared with those of the original solution. A decrease in the absorbance of paracetamol with respect to the irradiation time was used to determine the efficiency of the photocatalysts. Total organic carbon (TOC) analysis was carried out for the most active catalyst with an Analytik Jena multi N/C 3100 analyzer.

Photocatalytic H_2 Evolution: Sample Preparation. TiO_2 powder (5.0 mg, unless otherwise stated) was transferred into a glass sample vial (Chromacol 10-SV, Fisher) along with the reagent solution containing 0.1 M triethanolamine (TEOA) with pH 7.0 (3.0 mL, unless otherwise stated). Samples were capped with rubber septa, briefly vortexed, and agitated in a sonic bath for 20 min. Samples were purged with N_2 for 10 min prior to irradiation to deaerate the solution. Samples were irradiated using a solar light simulator (Thermo Oriel 92194-1000) equipped with an AM 1.5G filter (Newport) with an intensity of 1 sun. Samples were mounted in a quartz water bath maintained at 25 °C and stirred at 800 RPM. The sample headspace was subject to a constant purge of N_2 at a rate of 4 mL min^{-1} controlled by a mass flow controller (Bronkhorst). H_2 evolution was monitored by the online gas chromatographic analysis of the headspace stream.

Sample Analysis by Gas Chromatography. A Shimadzu Nexis GC-2030 gas chromatograph equipped with a barrier-discharge ionization detector (BID) and a molecular sieve column (5A PLOT capillary column, 30 m × 0.53 mm, 50 μm, kept at 140 °C) was used to quantify hydrogen produced in the process. The total run time of the method was 5 min. The GC was calibrated using calibration gas (2000 ppm H_2, BOC), diluted with N_2 at different ratios using a set of mass flow controllers (Bronkhorst) to provide known concentrations of H_2. Gas samples were programmed to auto-inject into the GC via a multiport stream selector valve directing the selected sample purge gas stream through a 2 mL sample loop before injection. H_2 evolution rates were calculated from the measured H_2 concentration in the purge gas and the purge gas flow rate. Cumulative H_2 production was calculated from the H_2 evolution rate and time elapsed since the previous measurement, assuming a constant H_2 evolution rate between time points. All analyses were performed in triplicates unless otherwise stated.

Computational Modeling. All density functional theory (DFT) calculations were performed by the projector-augmented wave method (PAW) implemented in the Vienna ab initio Simulation Package (VASP).[47−49] The Perdew−Burke−Ernzerhof (PBE) function within the generalized gradient approximation (GGA) was used to describe the exchange−correlation function.[50,51] A cut-off energy of 400 eV was used for the plane wave basis set. The energy and force convergence criteria for geometry optimization were set as 10^{-6} eV and 0.02 eV/Å, respectively. The Brillouin zone was sampled with a 2 × 2 × 1 Monkhorst−Pack k-point mesh.[52] The optimized lattice parameters of TiO_2 (001) and TiO_2 (101) are 11.36 Å × 11.36 Å × 13.17 Å and 10.92 Å × 15.14 Å × 9.81 Å, respectively. The vacuum space is larger than 10 Å to avoid an interlayer interaction. The onsite Coulombic interaction corrections approach (DFT + U) with U = 5 eV was employed to treat the 3d orbital electrons of Ti atoms.[53]

Recently, Kim et al.[54] experimentally and theoretically demonstrated that the adsorption energy of rutile TiO_2 can be tuned by a changeable Fermi level resulting in charged intermediates during chemisorption. In this regard, the Gibbs free energies of OER intermediates on an anatase TiO_2 (101) surface in this work were calculated using the following equation

$$\Delta G = \Delta E + \Delta \mathrm{ZPE} - T\Delta S + 0.059\mathrm{pH} + q(E_{\mathrm{VBM}} + \varepsilon_{\mathrm{F}}) - e\Delta\phi \quad (1)$$

where ΔE, ΔZPE, and ΔS are the adsorption energies, zero-point energies, and entropy difference, respectively, ε_F and E_{VBM} are the Fermi level and DFT-computed eigenvalue of the VBM energy level of anatase TiO_2 (101), respectively, and $\Delta\phi$ in the last term of eq 1 is the potential difference between the valence band maximum (VBM) and the water oxidation potential, which is added to take the potential energy change of photogenerated holes during oxidation.

RESULTS AND DISCUSSION

XRD analysis was performed to investigate the structural properties of the pristine TiO_2 and Ag/TiO_2 samples. As seen in Figure 1, the peaks of all of the samples at 2θ values of 25.5, 37.8, 48.0, 53.9, 55.1, 62.7, 68.8, 70.3, and 75.0° match the reflections from (101), (004), (200), (105), (211), (204), (116), (220), and (215) crystal planes of the tetragonal anatase phase of TiO_2 (JCPDS card no. 21-1217) with lattice constants a = 3.785 Å and c = 9.513 Å.[4] Despite the addition of Ag metal (0.5 and 1 wt %) as implants/dopants, the XRD patterns of the modified TiO_2 samples appeared similar to that of pristine TiO_2. This can be attributed to the small weight

https://doi.org/10.1021/acsomega.2c06657
ACS Omega 2023, 8, 1249−1261

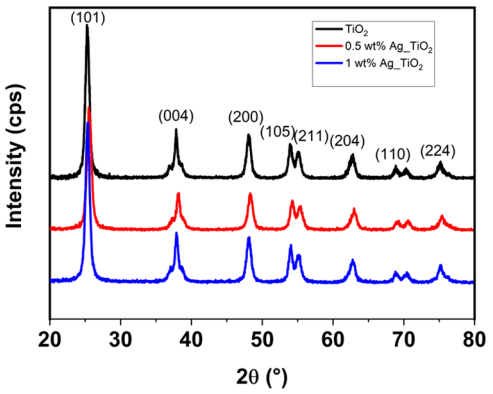

Figure 1. X-ray diffraction analysis of pristine and Ag nanoparticle-coated TiO_2 powders.

percentage of externally added atoms leading to a well-dispersed mix in the TiO_2 matrix, thereby unaffecting the crystalline structure.

The morphology and microstructure of the as-synthesized mesoporous pristine and doped TiO_2 were analyzed through TEM images. The TEM images of pure TiO_2 in Figure S3a showed that the TiO_2 particles were in the 10−15 nm size range, and these particles appear to be clustered together, which is confirmed by the high-resolution TEM micrograph shown in Figure S3a. Further, the clearly appearing lattice indicates the crystalline nature of the particles with a spacing of 3.5 Å, which corresponds to the (101) plane of tetragonal anatase TiO_2Figure S3b. Upon Ag nanoparticle deposition on TiO_2, the particle size and shape of the TiO_2 host significantly changed (Figure 2a). The particle size enhancement of TiO_2 from 10−15 to 80−100 nm might be due to the presence of inorganic moieties in the Ag nanoparticle solution. Mainly the traces of trisodium citrate may influence the TiO_2 particle growth. However, the origin of TiO_2 particle size enhancement is not clear. The Ag nanoparticles are randomly distributed on the TiO_2 surface, which leaves naked sites at TiO_2. These uncoated TiO_2 sites can allow access to both Ag and TiO_2 surface sites for photocatalytic reactions. Figure S4 shows that the (111) plane of face cubic center (FCC) Ag is clearly observed on the TiO_2 surface.

The chemical environment of pristine TiO_2 and Ag nanoparticle-coated TiO_2 was studied with XPS spectra (Figure 3a,b). Figure 3a,b shows the high-resolution XPS core spectra of Ti 2P and O 1S of pristine and nanoparticle-coated mesoporous TiO_2. In Figure 3a, Ti $2p_{3/2}$ and Ti $2p_{1/2}$ peaks are observed at binding energies of 458.7 and 464.5 eV, respectively. The difference in these binding energies is 5.8 eV which corresponds to the +4 oxidation state in mesoporous TiO_2.[55−57] The O 1s peak at 530 eV is perfectly symmetric without any shoulder at higher binding energies, suggesting the absence of different oxygen species in the mesoporous TiO_2. The binding energies of Ti $2p_{3/2}$, Ti $2p_{1/2}$, and O 1s peaks are in accordance with those reported for anatase TiO_2,[58] which is in good agreement with the XRD results. The XPS results of mesoporous TiO_2 were also compared with commercial P25 TiO_2 (Figure 3a,b). Figure 3b indicates that commercial P25 TiO_2 has a broader peak at 532.2 eV attributed to hydroxyl groups on the surface, which help to adsorb the water pollutants on the TiO_2 surface during the photocatalysis reactions. Interestingly, the peak shoulder broadening at 532.2 eV is missing in mesoporous TiO_2.

The Ag 3d high-resolution XPS spectra of Ag nanoparticle-coated mesoporous titania are depicted in Figure 3c. The Ag $3d_{5/2}$ and Ag $3d_{3/2}$ peaks are observed at binding energies of 368.1 and 374 eV, which we attribute to Ag^0.[59,60] Note that these two peaks are broad and could overlap with peaks attributed to Ag_2O and the electronic interaction between the metal and support. For Ag_2O, the binding energies of the Ag $3d_{5/2}$ and Ag $3d_{3/2}$ peaks are observed at 367.73 and 373.71 eV.[61] Gogoi et al.[37] attributed the lower binding energies of Ag $3d_{5/2}$ (366.45 eV) and Ag $3d_{3/2}$ (372.5 eV) to the electronic interaction between the metal and support by charge transfer at the metal−support interface. The Ag 3d peak intensities understandably increased with increasing Ag loading. It can be seen from Figure 3a that Ti 2p spectra shift to higher binding energies upon silver doping. We ascribe this shift to an increase in the effective positive charge of Ti owing to the electronic redistribution caused by the dopant, leading to a decrease in the Ti outer electron density, a reduction in the shielding effect, and an increase in the electron binding energy.[62,63] These effects are likely beneficial for enhancing photocatalytic activity. The O 1s spectra of Figure 3b show the appearance of the shoulder located at a binding energy of 532.2 eV after silver doping, which is attributed to OH groups on the surface.[64] Hydroxyl groups (OH^-) on the surface of the catalyst positively affect the photocatalytic activity.

With the increasing hydroxyl content on the surface of TiO_2, the surface becomes more likely to enhance the photocatalytic activity of TiO_2.[62] On the other hand, the increase in surface OH^- content could promote electron−hole separation, increasing the photocatalytic activity.[65,66] Further analyzing the C 1s spectra of Ag-coated TiO_2 (Figure S5) shows an increased intensity of the peak at a binding energy of 289.7 eV compared with pure TiO_2, which could be ascribed to the presence of citrate (reducing agent) adsorbed on silver nanoparticles, which is in good agreement with Raman characterization results (Figure S6).

The optical bandgap of pristine and Ag/TiO_2 was estimated from UV−vis diffuse reflectance spectra given by $(\alpha h\upsilon)^{1/n} = A(h\upsilon - E_g)$, where E_g is the optical bandgap energy, α is the absorption coefficient, h is the Planck's constant, υ is the frequency of light, A is the proportionality constant and n are 1/2 and 2, respectively for direct and indirect bandgap semiconductors. Since TiO_2 is an indirect bandgap semiconductor, a plot between photon energy $h\upsilon$ and $(\alpha h\upsilon)^{1/2}$ was constructed, and E_g was estimated by extrapolating the linear portion of the y-axis onto the x-axis, as shown in Figure 4. The bandgap energy of pure TiO_2 is reduced from 3.1 to 2.91 eV by Ag nanoparticle coating.

The porosity of different photocatalysts was studied by BET analysis. Figure 5 shows typical irreversible type IV N_2 adsorption isotherms with an H1 hysteresis loop[67] for pristine and Ag/TiO_2. The surface area and pore volume of the pure and Ag/TiO_2 are presented in Table S1. It is worth noting that the mesoporous TiO_2 synthesized in this work exhibited a high specific surface area of 102 m^2/g, which is 2.5 times higher than that of commercial P25 TiO_2 (56 m^2/g).[68,69] Also, it resulted in a significantly higher pore volume of 0.325 cm^3/g compared with commercial P25 TiO_2 (0.02 cm^3/g).[68] It is inferred that the P123 surfactant templates effectively induced the mesoporous network at TiO_2, which is the reason for the increased surface area compared with the commercial P25 TiO_2 powder. As can be seen from Table S1, the textural properties of pure mesoporous TiO_2 are maintained, whatever

https://doi.org/10.1021/acsomega.2c06657
ACS Omega 2023, 8, 1249−1261

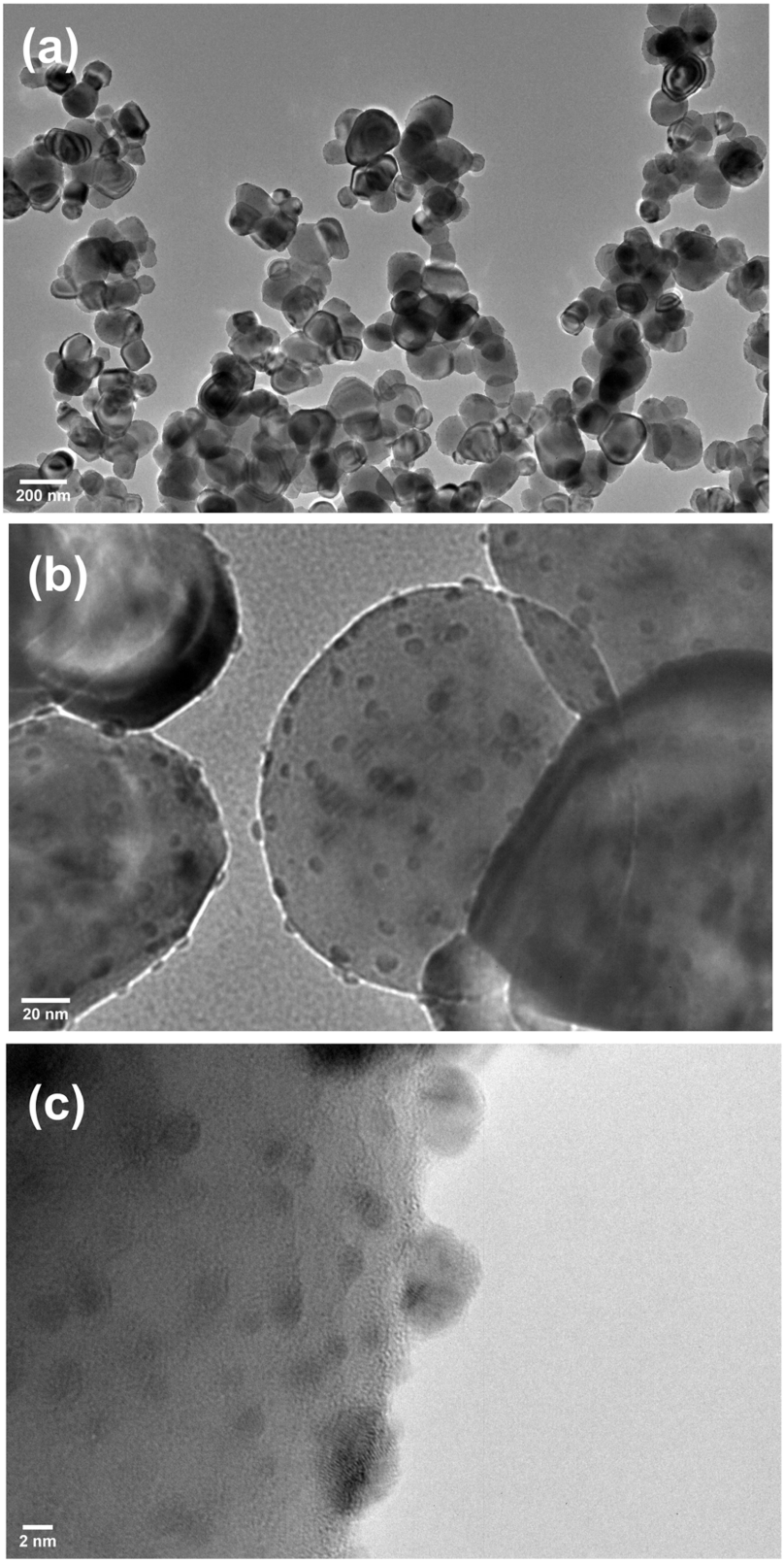

Figure 2. HRTEM images of the Ag (1 wt %) nanoparticle-coated TiO_2 powder at different magnification scales (a) 200 nm, (b) 20 nm, and (c) 2 nm.

the mass percentage of Ag nanoparticle coating. The slight decrease in the specific surface area after doping with Ag is ascribed to the clogging of support pores by silver that makes them inaccessible for nitrogen adsorption.[70]

The photocatalytic activity of pristine TiO_2 and Ag/TiO_2 photocatalysts was evaluated through the photocatalytic degradation of paracetamol in water under natural sunlight. The experimental setup is shown in Figure S2. UV−vis

https://doi.org/10.1021/acsomega.2c06657
ACS Omega 2023, 8, 1249−1261

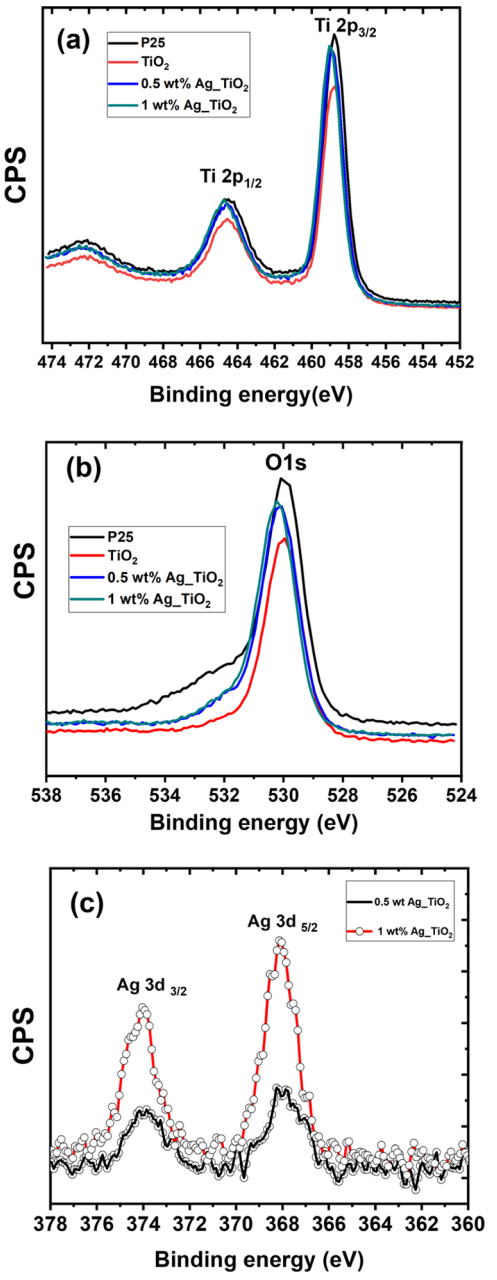

Figure 3. XPS core spectra of (a) Ti 2p, (b) O 1s, and (c) Ag 3d. The results of panels (a and b) are compared with those of the commercial P25 powder.

absorption spectra corresponding to the visible-light-driven photocatalytic degradation of paracetamol in the presence of 1 wt % Ag/TiO_2 are presented in Figure 6a, wherein the consistent reduction in the intensity of the characteristic absorption peak (244 nm) of paracetamol is indicative of the decrease in its concentration. The C/C_0 values for all of the photocatalyst samples are estimated and presented in Figure 6b as a function of irradiation time. As seen in Figure 6b, the photodegradation of paracetamol was negligible under visible-light irradiation only in the absence of any photocatalyst. Figure 6b shows that the absorbance of the paracetamol solution (10 mg/L) after stirring with TiO_2-based photocatalysts in the dark for 30 min is nearly constant. This indicates that the adsorption of paracetamol on the catalyst surface is negligible due to the neutrality of the paracetamol

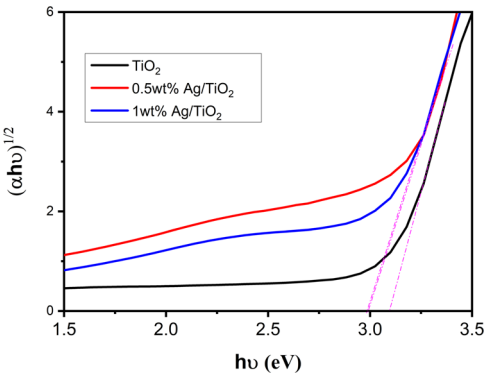

Figure 4. Plots of the Kubelka–Munk function versus the energy of the absorbed light for pure and Ag nanoparticle-coated mesoporous TiO_2.

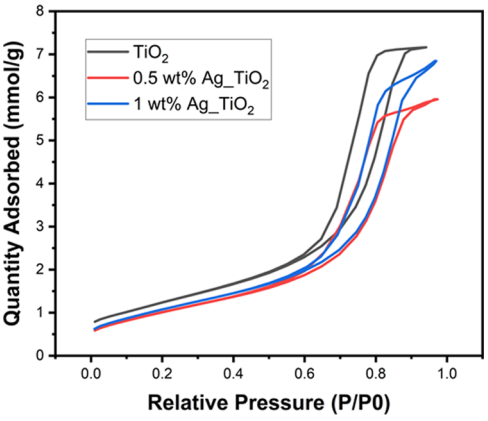

Figure 5. Adsorption–desorption isotherms of nitrogen on pristine and Ag nanoparticle-coated mesoporous TiO_2 at 77 K.

molecule. The degradation performance of Ag/TiO_2 was compared against N- and La-doped TiO_2, as shown in Figure 6b, to investigate the effect of other dopants (nonmetal and rare earth elements) on the photocatalytic performance of mesoporous TiO_2. Note that the N- and La-doping at TiO_2 are not identical in quantity to Ag nanoparticles. The 2 wt % La-doped mesoporous TiO_2 resulted in higher degradation of paracetamol compared to pristine TiO_2. Earlier studies have reported that La-doping increased the adsorption capacity of organic compounds and inhibited the e^-–h^+ recombination during the photocatalytic reaction.[71,72]

In the case of N-doped TiO_2, the improved photocatalytic activity compared to pristine TiO_2 resulted from the slightly extended absorption in the visible-light range, indicating that more photogenerated electrons and holes can participate in the photocatalytic reactions under visible light[73−75] (Figure S6). The improvement of visible-light absorption after nitrogen doping can be attributed to bandgap narrowing, the creation of an impurity energy level, or even oxygen vacancies.[76,77]

In general, the toxic organic molecules can be degraded via photocatalysis, but their byproducts may require additional time to completely degrade into nontoxic minerals, which is safer for discharge into water bodies.[78] Analyzing changes to the total organic carbon (TOC) in the reaction system ensured the complete removal of toxic organic molecules.[78] Therefore, the photocatalytic mineralization of paracetamol using 1 wt % Ag/TiO_2 was evaluated. It implied that, although 10 ppm paracetamol was completely degraded (~100%) within 120

https://doi.org/10.1021/acsomega.2c06657
ACS Omega 2023, 8, 1249−1261

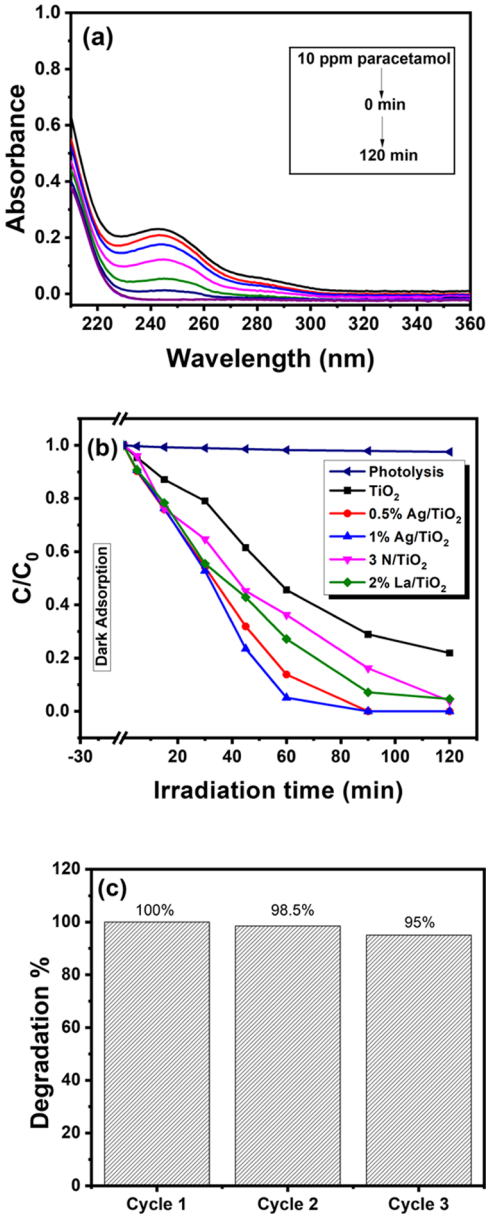

Figure 6. (a) UV−Visible absorption spectra of paracetamol photodegradation using 1 wt %Ag/TiO_2 and (b) paracetamol photocatalytic degradation over pristine and Ag nanoparticles-coated mesoporous TiO_2 under natural solar light irradiation. The results were compared with N- and La-doped TiO_2 powder samples. (c) Recycling photocatalytic degradation of paracetamol over 1 wt % Ag/TiO_2 under natural solar light irradiation.

min, the intermediate organic byproducts took up to 300 min to mineralize (98%, as measured using a TOC analyzer). In addition to higher photocatalytic efficiency, the stability of the photocatalyst against photocorrosion is a crucial factor that is usually considered for deciding its employability for industrial applications. Therefore, for studying the effect of photocorrosion on 1 wt % Ag/TiO_2, the photocatalytic degradation of paracetamol was performed repeatedly for three continuous cycles by reusing the catalyst after its separation from the residual slurry through centrifugation. As evident from Figure 6c, there is an insignificant decline in the photodegradation efficiency, which could be attributed to the loss of the photocatalyst during each round of centrifugation and rinsing.

Due to technical difficulties in outdoor sunlight irradiation experiments for measuring the hydrogen gas generation via gas chromatography, we demonstrated H_2 gas generation indoors using simulated solar irradiation (AM 1.5 G). The aqueous paracetamol (10 ppm)-based electrolyte similar to the above experiment was tested in photocatalytic hydrogen generation reactions, but there is no hydrogen generation observed, which may be due to the inadequate concentration of paracetamol needed to produce donors or the slowest oxidation rate of paracetamol is not enough to produce H^+. Therefore, we added an organic sacrificial agent (TEOA) along with paracetamol, experiments were repeated with different photocatalysts, and the corresponding hydrogen gas generation was measured for 14 h. The results are presented in Figure 7. It can

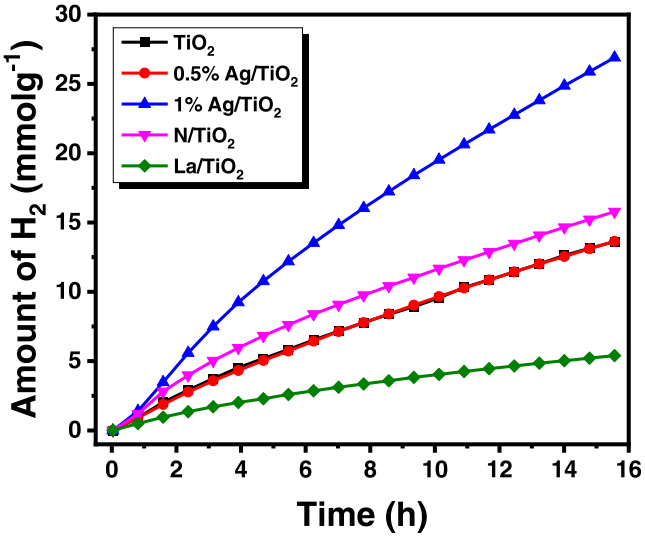

Figure 7. Photocatalytic H_2 production using different photocatalysts measured at 1 sun irradiation. Note that the electrolyte contains paracetamol (10 ppm) and TEOA, a sacrificial agent.

be seen from this figure that the H_2 production is almost linear with the reaction time. We expected paracetamol degradation alongside hydrogen gas evolution to be possible, but we did not verify it.

For the 1 wt % Ag/TiO_2 catalyst, the H_2 production rate was exalted after 3 h of reaction. The photocatalytic activity of the samples varies in the following decreasing order: 1 wt %Ag/TiO_2 > 0.5 wt %Ag/TiO_2 > TiO_2. It is interesting to note that 1 wt % Ag/mesoporous TiO_2 is the most active catalyst for both the photodegradation of paracetamol and H_2 production. The highest photocatalytic hydrogen evolution activity achieved was 1729 μmol H_2 g^{-1} h^{-1}, which largely exceeded that obtained over bare mesoporous TiO_2 (875 μmol H_2 g^{-1} h^{-1}). On the other hand, for the other catalysts, the ranking of activities is different from that obtained for the photodegradation of paracetamol.

Note that 2 wt % La/TiO_2 was less active than TiO_2. Liu et al.[79] reported that the proper amount of lanthanum-doped TiO_2 enhanced the photocatalytic hydrogen production, but excessive lanthanum ions inhibited the activity by blocking active sites on TiO_2. In our case, we cannot advance this explanation since 2 wt % La/TiO_2 was more active than TiO_2 for paracetamol degradation. The negative effect of lanthanum could be explained by the fact that lanthanum shifts the conduction band maximum (CBM) below the H^+/H_2

https://doi.org/10.1021/acsomega.2c06657
ACS Omega 2023, 8, 1249−1261

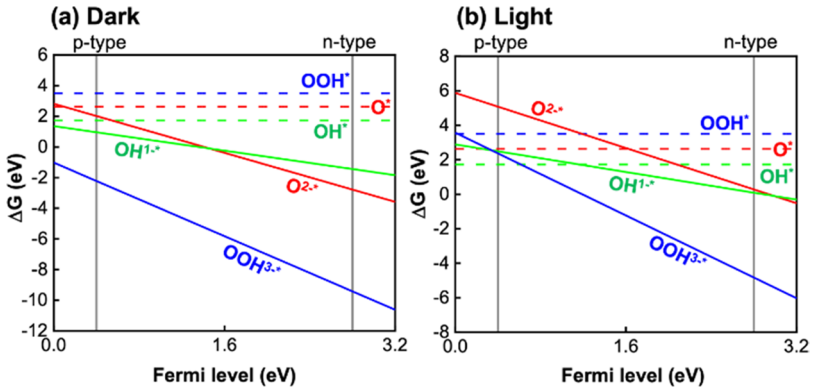

Figure 8. Gibbs free energy graph as a function of the Fermi level of anatase TiO_2 (101) for OER at pH 7 under (a) dark and (b) light irradiation conditions.

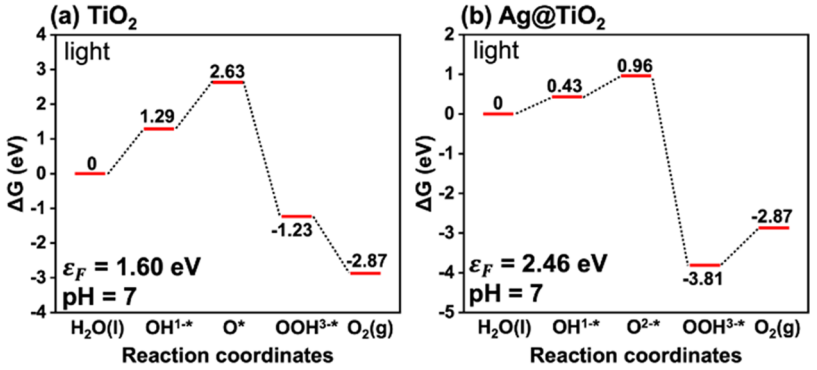

Figure 9. Gibbs free energy diagrams of (a) TiO_2 and (b) Ag@TiO_2 under UV light irradiation.

reduction potential, which means that it does not meet the requirement for H_2 evolution.[80,81] This result is in contradiction with those of Shwetharan et al., who used La-TiO_2 prepared by direct synthesis using La_2O_3 as the lanthanum source.[82] In our study, lanthanum is not incorporated into the lattice of TiO_2, unlike what was reported by Shwetharan et al., which could explain this contradictory result. In the case of N doping, TiO_2 performed better for hydrogen evolution due to the enhancement of visible-light activity at TiO_2. But its paracetamol degradation performance was inferior to La-doped TiO_2, suggesting that its valence band position may be less positive than the pollutant oxidation potential.

Overall, we proved the suitability of Ag nanoparticle-coated mesoporous TiO_2 photocatalysts for simultaneous pharmaceutical water pollutant degradation and hydrogen generation. The results presented in Figures 6b and 7 show paracetamol degradation and hydrogen gas evolution on the same Ag/TiO_2 photocatalyst. To understand the effect of Ag metal loading on the anatase TiO_2 (101) surface on the catalytic reactivity of the oxygen evolution reaction (OER) process at pH 7 under UV light irradiation, we calculated Gibbs free energies of OER intermediates using eq 1 (Figure 8). We considered that the adsorbate intermediates of OER (OH*, O*, and OOH*) can be charged due to the charge transfer between the anatase TiO_2 (101) surface and the adsorbates. All possible charge states of adsorbates were considered for modeling and the Gibbs free energy calculations.

Then, we compared two cases of surface kinetic energies (Gibbs free energy diagram): anatase TiO_2 (i) without Ag metal loading (ii) with Ag metal loaded on the surface (Ag@TiO_2) (Figure 9). Considering that the typical upward band bending of an n-type semiconductor is nearly 1 eV and the average Fermi level of anatase TiO_2 lies at 2.6 eV,[83] the surface Fermi level of bare TiO_2 was assumed to be 1.6 eV (Figure 9a). In general, the work function of a metal is a decisive factor for the band bending at the interface of a metal−semiconductor heterojunction. The difference in the work function between pristine n-type anatase TiO_2 (~4.7 eV) and Ag (4.74 eV) is tiny (<0.1 eV) compared to the band bending energy of the bare anatase TiO_2(101) surface (~1 eV) induced by the space charge of TiO_2.[83−85]

Therefore, the surface Fermi levels of the two materials are aligned at the equilibrium state, resulting in band bending at the interface. According to the Gibbs free energy graph, relevant reactive intermediates in the water oxidation mechanisms are OH*, O*, and OOH* intermediates, where * indicates the surface-adsorbed states of OH, O, and OOH. The reaction steps can be explained as[86,87]

$$* + H_2O \rightarrow OH^* + (H^+ + e^-) \quad (2)$$

$$OH^* \rightarrow O^* + (H^+ + e^-) \quad (3)$$

$$O^* + H_2O \rightarrow OOH^* + (H^+ + e^-) \quad (4)$$

$$^*OOH \rightarrow O_2 + (H^+ + e^-) \quad (5)$$

The reactive intermediate O* can be classified as dangling O* (O1*) and surface-bound peroxo species (O2*). The stability of O* depends on the semiconductor catalyst.[87] In accordance with Malik et al.,[86] when $\Delta G_{OH^*} > 2.73$ eV, the photocatalyst will produce •OH in the electrolyte via the one-electron transfer process. Also, they suggested that peroxo O2*

https://doi.org/10.1021/acsomega.2c06657
ACS Omega 2023, 8, 1249−1261

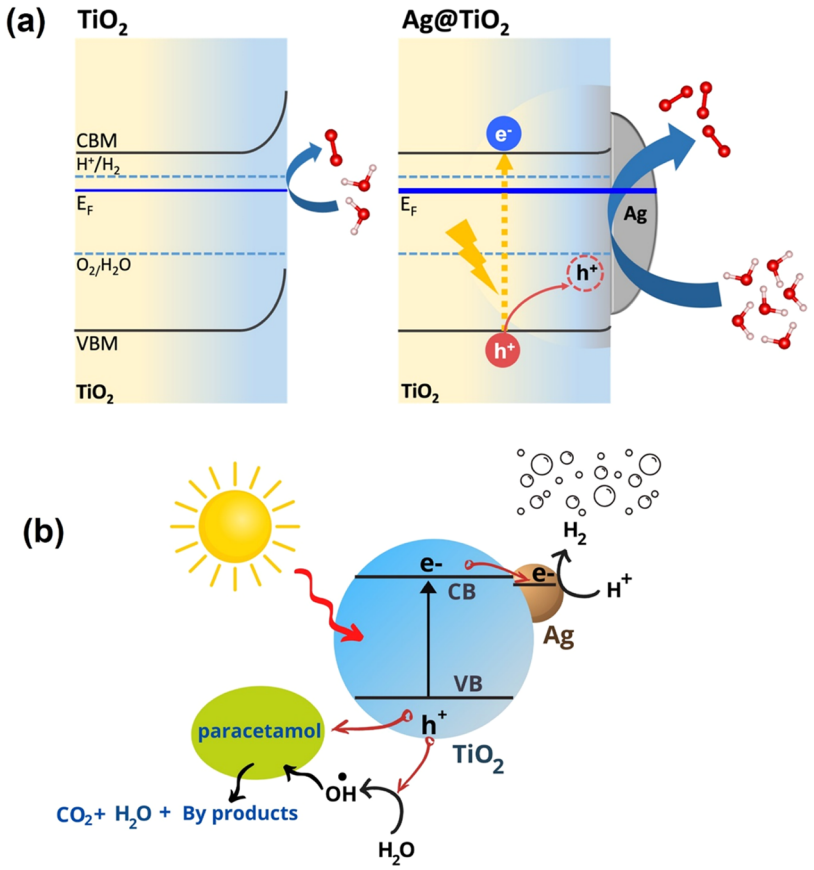

Figure 10. Schematic illustration of (a) energy band diagrams of pristine anatase TiO_2 and Ag@TiO_2 and (b) the photocatalytic degradation of paracetamol and hydrogen gas evolution on Ag/TiO_2 photocatalysts.

intermediate species are more stable than dangling O1* species, which is in favor of the two-electron process to form H_2O_2. Furthermore, the product ratio and selectivity (H_2O_2 vs. O_2) will be dictated by the kinetic barriers rather than thermodynamic applied potentials.[86] From Figure 9(b), the energy barrier in the rate-determining steps of the OER process was lowered at Ag/TiO_2 (ε_F = 2.46 eV) by 0.86 eV in comparison to that of bare anatase TiO_2 (ε_F = 1.60 eV). Ultraviolet photoelectron spectra (Figure S7) show that the CB maximum position changes, confirming that the work function of mesoporous TiO_2 was modified by Ag deposition. We conclude that Ag metal loading can adjust the band bending and Fermi level of an anatase TiO_2 surface, leading to the improvement in the reactivity on the surface of TiO_2, thus promoting the accessibility of photoelectrons at the conduction band where H^+ is reduced to hydrogen gas. On the other hand, Figure 9a,b shows that OH^{1-}* intermediate formation required smaller step change of ΔG when Ag nanoparticle was deposited on TiO_2. This indicates the higher probability of paracetamol oxidation with Ag/TiO_2.

Based on the experimental and theoretical results, the process of pharmaceutical water pollutant degradation and hydrogen gas generation at Ag/TiO_2 photocatalysts is schematically explained in Figure 10. Note that examining paracetamol degradation pathways is not the focus of our work; however, it is worth investigating the byproducts and their potentially toxic nature.[88−90]

CONCLUSIONS

Mesoporous TiO_2 was synthesized via a gram-scale chemical route using the P123 surfactant as a template. Presynthesized Ag nanoparticles were successfully coated onto TiO_2, and structural and textural properties of the resultant Ag/TiO_2 composite were examined. This modified Ag/TiO_2 showed higher photocatalytic performance for paracetamol degradation and H_2 production compared with pristine TiO_2. The high activity of mesoporous Ag/TiO_2 can be attributed to several factors: (a) strong inhibition of the e^-−h^+ recombination due to the Schottky barrier formation at the TiO_2−Ag interface,[91] (b) hydroxyl group formation facilitating pollutant adsorption on the TiO_2 surface, and (c) extended visible-light activity. Over this most active catalyst, 100% degradation of paracetamol was reached after only 90 min with 98% total organic content (TOC) abatement and 1729 μmol H_2 g^{-1} h^{-1} was achieved for hydrogen generation, which largely exceeds that obtained over pristine mesoporous TiO_2 (875 μmol H_2 g^{-1} h^{-1}). Moreover, 1 wt % Ag/mesoporous TiO_2 was stable, and Ag effectively optimized the Fermi level of the TiO_2 surface for higher reactivity. Thus, Ag/TiO_2 is an attractive photocatalyst candidate for tandem environmental remediation and hydrogen generation under solar irradiation. Conversely, comparative tests with other dopants such as N- and Ln-doped TiO_2 showed enhanced performance in either pollutant degradation or hydrogen evolution over pristine TiO_2, but not for both processes. These results suggest that for further research on analyzing the surface functionality of photocatalysts and determining energy levels with respect to the HER and OER

https://doi.org/10.1021/acsomega.2c06657
ACS Omega 2023, 8, 1249−1261

potential, charge transfer resistance at semiconductor catalyst/electrolyte interfaces will help to further optimize doped TiO_2 for effective simultaneous photocatalytic reactions. The gram-scale-synthesized Ag nanoparticle-doped TiO_2 photocatalyst powder from this work can be coated on substrates to facilitate photocatalyst recycling for batch reactors.

■ ASSOCIATED CONTENT

Supporting Information

The Supporting Information is available free of charge at https://pubs.acs.org/doi/10.1021/acsomega.2c06657.

Photography of TiO_2 and Ag/TiO_2 photocatalysts, TEM images, Raman spectra, optical bandgap results, BET results, and UPS results (PDF)

■ AUTHOR INFORMATION

Corresponding Authors

Sudhagar Pitchaimuthu − *Research Centre for Carbon Solutions, Institute of Mechanical and Processing Engineering, School of Engineering & Physical Science, Heriot-Watt University, Edinburgh EH14 4AS, United Kingdom;* orcid.org/0000-0001-9098-8806; Email: S.Pitchaimuthu@hw.ac.uk

Hajer Azzi − *Laboratoire de Catalyse et Synthèse en Chimie Organique, Université de Tlemcen, Tlemcen 13000, Algeria; Institut des Sciences et de la Technologie, Université d'Ain Témouchent, 46000 Ain Témouchent, Algeria;* Email: catalyse030781@yahoo.fr

Authors

Yassine Cherif − *Laboratoire de Catalyse et Synthèse en Chimie Organique, Université de Tlemcen, Tlemcen 13000, Algeria*

Kishore Sridharan − *Department of Nanoscience and Technology, School of Physical Sciences, University of Calicut, P. O. Thenhipalam 673635, India;* orcid.org/0000-0002-2099-2962

Seulgi Ji − *Theoretical Materials & Chemistry Group, Institute of Inorganic Chemistry, University of Cologne, 50939 Cologne, Germany*

Heechae Choi − *Theoretical Materials & Chemistry Group, Institute of Inorganic Chemistry, University of Cologne, 50939 Cologne, Germany;* orcid.org/0000-0002-9390-6607

Michael G. Allan − *Department of Chemistry, Swansea University, Swansea SA2 8PP, United Kingdom*

Sihem Benaissa − *Institut des Sciences et de la Technologie, Université d'Ain Témouchent, 46000 Ain Témouchent, Algeria;* Present Address: High National School of Public Works, BP 32 Rue Sidi Garidi, Kouba, Alger, Algérie

Karima Saidi-Bendahou − *Laboratoire de Catalyse et Synthèse en Chimie Organique, Université de Tlemcen, Tlemcen 13000, Algeria*

Lois Damptey − *School of Engineering & Innovation, The Open University, Milton Keynes MK7 6AA, United Kingdom*

Camila Silva Ribeiro − *School of Engineering & Innovation, The Open University, Milton Keynes MK7 6AA, United Kingdom*

Satheesh Krishnamurthy − *School of Engineering & Innovation, The Open University, Milton Keynes MK7 6AA, United Kingdom;* orcid.org/0000-0001-7237-9206

Sanjay Nagarajan − *Department of Chemical Engineering, University of Bath, Bath BA2 7AY, United Kingdom;* orcid.org/0000-0003-2678-693X

M. Mercedes Maroto-Valer − *Research Centre for Carbon Solutions, Institute of Mechanical and Processing Engineering, School of Engineering & Physical Science, Heriot-Watt University, Edinburgh EH14 4AS, United Kingdom*

Moritz F. Kuehnel − *Department of Chemistry, Swansea University, Swansea SA2 8PP, United Kingdom; Fraunhofer Institute for Wind Energy Systems IWES, 06237 Leuna, Germany;* orcid.org/0000-0001-8678-3779

Complete contact information is available at: https://pubs.acs.org/10.1021/acsomega.2c06657

Author Contributions

Y.C., H.A., and S.P. conceived the idea and demonstrated the experiments. S.B. and K.B. supported the materials synthesis and optical experiments. K.S. and S.N. contributed to the draft preparation and data analysis. M.G.A. and M.F.K. conducted the photocatalytic hydrogen generation experiments and contributed to the draft preparation. L.A.D., C.S.R., and S.K. contributed to TEM image recording and XPS experiments. S.P. coordinated the manuscript preparation and data analysis. M.M.V., S.N., and M.F.K. contributed to draft corrections. S.J. and H.C. demonstrated the theoretical simulation work.

Funding

S.P. and M.F.K. acknowledge support from the Welsh Government (Sêr Cymru III − Tackling Covid-19, Project 076 ReCoVir). This work was supported by EPSRC through a DTA studentship to M.G.A (EP/R51312X/1) and a capital investment grant to M.F.K. (EP/S017925/1). We thank Swansea University for providing startup funds to M.F.K.

Notes

The authors declare no competing financial interest.

■ ACKNOWLEDGMENTS

The authors Y.C. and H.J. would like to thank the Algerian DGRST-MESRS and the University of Tlemcen for financial support. SP thanks Heriot-Watt University for the Seed Grant support. S.J. and H.C. thank the University of Cologne and the Excellence Cluster "Quantum Matter and Materials" for the infrastructural support. S.K. acknowledges the Royal Academy of Engineering Newton Fund and European Commission project id: 958491—Smart innovative system for recycling wastewater and creating closed loops in textile manufacturing industrial processes.

■ ABBREVIATIONS USED

BID, barrier-discharge ionization detector
CBM, conduction band maximum
DFT, density functional theory
GC, gas chromatography
GGA, generalized gradient approximation
HRTEM, high-resolution transmission electron microscopy
JCPDS, joint committee on powder diffraction standards
LSPR, localized surface plasmon resonance
OER, oxygen evolution reaction
Ov, oxygen vacancies
PAW, projector-augmented wave method
PBE, Perdew−Burke−Ernzerhof
PPCP, pharmaceutical and personal care products
TEOA, triethanolamine

https://doi.org/10.1021/acsomega.2c06657
ACS Omega 2023, 8, 1249−1261

TOC, total organic carbon
UPS, ultraviolet photoelectron spectroscopy
VASP, Vienna ab initio simulation package
VBM, valence band maximum
XPS, X-ray photoelectron spectroscopy
XRD, X-ray diffraction

REFERENCES

(1) Schwarzenbach, R. P.; Egli, T.; Hofstetter, T. B.; von Gunten, U.; Wehrli, B. Global Water Pollution and Human Health. *Annu. Rev. Environ. Resour.* **2010**, *35*, 109−136.
(2) Davies, K. R.; Cherif, Y.; Pazhani, G. P.; Anantharaj, S.; Azzi, H.; Terashima, C.; Fujishima, A.; Pitchaimuthu, S. The upsurge of photocatalysts in antibiotic micropollutants treatment: Materials design, recovery, toxicity and bioanalysis. *J. Photochem. Photobiol., C* **2021**, *48*, No. 100437.
(3) Jiao, Z.; Zhang, Y.; Ouyang, S.; Yu, H.; Lu, G.; Ye, J.; Bi, Y. BiAg alloy nanospheres: a new photocatalyst for H2 evolution from water splitting. *ACS Appl. Mater. Interfaces* **2014**, *6*, 19488−19493.
(4) Chaker, H.; Chérif-Aouali, L.; Khaoulani, S.; Bengueddach, A.; Fourmentin, S. Photocatalytic degradation of methyl orange and real wastewater by silver doped mesoporous TiO2 catalysts. *J. Photochem. Photobiol., A* **2016**, *318*, 142−149.
(5) Ahmad, K.; Ghatak, H. R.; Ahuja, S. A review on photocatalytic remediation of environmental pollutants and H2 production through water splitting: A sustainable approach. *Environ. Technol. Innovation* **2020**, *19*, No. 100893.
(6) Zhang, J.; Li, L.; Xiao, Z.; Liu, D.; Wang, S.; Zhang, J.; Hao, Y.; Zhang, W. Hollow sphere TiO2−ZrO2 prepared by self-assembly with polystyrene colloidal template for both photocatalytic degradation and H2 evolution from water splitting. *ACS Sustainable Chem. Eng.* **2016**, *4*, 2037−2046.
(7) Varma, K. S.; Tayade, R. J.; Shah, K. J.; Joshi, P. A.; Shukla, A. D.; Gandhi, V. G. Photocatalytic degradation of pharmaceutical and pesticide compounds (PPCs) using doped TiO2 nanomaterials: A review. *Water-Energy Nexus* **2020**, *3*, 46−61.
(8) Bhatia, V.; Dhir, A. Transition metal doped TiO2 mediated photocatalytic degradation of anti-inflammatory drug under solar irradiations. *J. Environ. Chem. Eng.* **2016**, *4*, 1267−1273.
(9) Mathew, S.; Ganguly, P.; Kumaravel, V.; Bartlett, J.; Pillai, S. C.Solar Light-induced Photocatalytic Degradation of Pharmaceuticals in Wastewater Treatment. In *Nano-Materials as Photocatalysts for Degradation of Environmental Pollutants*, Singh, P.; Borthakur, A.; Mishra, P. K.; Tiwary, D., Eds.; Elsevier, 2020; Chapter 4, pp 65−78.
(10) Tayade, R. J.; Kulkarni, R. G.; Jasra, R. V. Transition Metal Ion Impregnated Mesoporous TiO2 for Photocatalytic Degradation of Organic Contaminants in Water. *Ind. Eng. Chem. Res.* **2006**, *45*, 5231−5238.
(11) Xiong, Z.; Ma, J.; Ng, W. J.; Waite, T. D.; Zhao, X. S. Silver-modified mesoporous TiO2 photocatalyst for water purification. *Water Res.* **2011**, *45*, 2095−2103.
(12) Lin, C. J.; Yang, W.-T.; Chou, C.-Y.; Liou, S. Y. H. Hollow mesoporous TiO2 microspheres for enhanced photocatalytic degradation of acetaminophen in water. *Chemosphere* **2016**, *152*, 490−495.
(13) Alvarez-Corena, J. R.; Bergendahl, J. A.; Hart, F. L. Advanced oxidation of five contaminants in water by UV/TiO2: Reaction kinetics and byproducts identification. *J. Environ. Manage.* **2016**, *181*, 544−551.
(14) Jin-hui, Z. Research on UV/TiO2 Photocatalytic Oxidation of Organic Matter in Drinking Water and Its Influencing Factors. *Procedia Environ. Sci.* **2012**, *12*, 445−452.
(15) Wu, Q.; Zhao, J.; Qin, G.; Wang, C.; Tong, X.; Xue, S. Photocatalytic reduction of Cr(VI) with TiO2 film under visible light. *Appl. Catal., B* **2013**, *142−143*, 142−148.
(16) Sudhagar, P.; Devadoss, A.; Nakata, K.; Terashima, C.; Fujishima, A. Enhanced Photoelectrocatalytic Water Splitting at Hierarchical Gd^{3+}:TiO_2 Nanostructures through Amplifying Light Reception and Surface States Passivation. *J. Electrochem. Soc.* **2015**, *162*, H108−H114.
(17) Naldoni, A.; Altomare, M.; Zoppellaro, G.; Liu, N.; Kment, Š.; Zbořil, R.; Schmuki, P. Photocatalysis with Reduced TiO2: From Black TiO2 to Cocatalyst-Free Hydrogen Production. *ACS Catal.* **2019**, *9*, 345−364.
(18) Do, H. H.; Nguyen, D. L. T.; Nguyen, X. C.; Le, T.-H.; Nguyen, T. P.; Trinh, Q. T.; Ahn, S. H.; Vo, D.-V. N.; Kim, S. Y.; Le, Q. V. Recent progress in TiO2-based photocatalysts for hydrogen evolution reaction: A review. *Arabian J. Chem.* **2020**, *13*, 3653−3671.
(19) Yang, S.; Tang, W.; Ishikawa, Y.; Feng, Q. Synthesis of titanium dioxide with oxygen vacancy and its visible-light sensitive photocatalytic activity. *Mater. Res. Bull.* **2011**, *46*, 531−537.
(20) Hirakawa, H.; Hashimoto, M.; Shiraishi, Y.; Hirai, T. Photocatalytic Conversion of Nitrogen to Ammonia with Water on Surface Oxygen Vacancies of Titanium Dioxide. *J. Am. Chem. Soc.* **2017**, *139*, 10929−10936.
(21) Hao, Y.-n.; Chen, T.; Zhang, X.; Zhou, H.; Ma, Y. Ti-Ti σ bond at oxygen vacancy inducing the deep defect level in anatase TiO2 (101) surface. *J. Chem. Phys.* **2019**, *150*, No. 224702.
(22) Wang, Y.; Zhang, M.; Lv, S.; Li, X.; Wang, D.; Song, C. Photogenerated Oxygen Vacancies in Hierarchical Ag/TiO2 Nanoflowers for Enhanced Photocatalytic Reactions. *ACS Omega* **2020**, *5*, 13994−14005.
(23) Bi, X.; Du, G.; Kalam, A.; Sun, D.; Yu, Y.; Su, Q.; Xu, B.; Al-Sehemi, A. G. Tuning oxygen vacancy content in TiO2 nanoparticles to enhance the photocatalytic performance. *Chem. Eng. Sci.* **2021**, *234*, No. 116440.
(24) Pedroza-Herrera, G.; Medina-Ramírez, I. E.; Lozano-Álvarez, J. A.; Rodil, S. E. Evaluation of the Photocatalytic Activity of Copper Doped TiO2 nanoparticles for the Purification and/or Disinfection of Industrial Effluents. *Catal. Today* **2020**, *341*, 37−48.
(25) Armaković, S. J.; Grujić-Brojčin, M.; Šćepanović, M.; Armaković, S.; Golubović, A.; Babić, B.; Abramović, B. F. Efficiency of La-doped TiO2 calcined at different temperatures in photocatalytic degradation of β-blockers. *Arabian J. Chem.* **2019**, *12*, 5355−5369.
(26) Zhu, X.; Pei, L.; Zhu, R.; Jiao, Y.; Tang, R.; Feng, W. Preparation and characterization of Sn/La co-doped TiO2 nanomaterials and their phase transformation and photocatalytic activity. *Sci. Rep.* **2018**, *8*, No. 12387.
(27) Kumar, A.; Choudhary, P.; Kumar, A.; Camargo, P. H. C.; Krishnan, V. Recent Advances in Plasmonic Photocatalysis Based on TiO2 and Noble Metal Nanoparticles for Energy Conversion, Environmental Remediation, and Organic Synthesis. *Small* **2022**, *18*, No. 2101638.
(28) Kumar, A.; Choudhary, P.; Krishnan, V. Selective and efficient aerobic oxidation of benzyl alcohols using plasmonic Au-TiO2: Influence of phase transformation on photocatalytic activity. *Appl. Surf. Sci.* **2022**, *578*, No. 151953.
(29) Kumar, A.; Shankar, K. R.; Kumar, A.; Harith, G.; Krishnan, V. Controlling the kinetics of visible-light-induced photocatalytic performance of gold decorated graphitic carbon nitride nanocomposite using different proteins. *J. Environ. Chem. Eng.* **2021**, *9*, No. 105147.
(30) Kumar, A.; Singla, Y.; Sharma, M.; Bhardwaj, A.; Krishnan, V. Two dimensional S-scheme Bi2WO6−TiO2−Ti3C2 nanocomposites for efficient degradation of organic pollutants under natural sunlight. *Chemosphere* **2022**, *308*, No. 136212.
(31) Zhang, W.; Ma, Y.; Zhu, X.; Liu, S.; An, T.; Bao, J.; Hu, X.; Tian, H. Fabrication of Ag decorated g-C3N4/LaFeO3 Z-scheme heterojunction as highly efficient visible-light photocatalyst for degradation of methylene blue and tetracycline hydrochloride. *J. Alloys Compd.* **2021**, *864*, No. 158914.
(32) Tian, H.; Wan, C.; Xue, X.; Hu, X.; Wang, X. Effective Electron Transfer Pathway of the Ternary TiO2/RGO/Ag Nanocomposite with Enhanced Photocatalytic Activity under Visible Light. *Catalysts* **2017**, *7*, 156.
(33) Tian, H.; Shen, K.; Hu, X.; Qiao, L.; Zheng, W. N, S co-doped graphene quantum dots-graphene-TiO2 nanotubes composite with

https://doi.org/10.1021/acsomega.2c06657
ACS Omega 2023, 8, 1249−1261

enhanced photocatalytic activity. *J. Alloys Compd.* **2017**, *691*, 369−377.
(34) Meng, Z.; Zhou, B.; Xu, J.; Li, Y.; Hu, X.; Tian, H. Heterostructured Nitrogen and Sulfur co-doped Black TiO2/g-C3N4 Photocatalyst with Enhanced Photocatalytic Activity. *Chem. Res. Chin. Univ.* **2020**, *36*, 1045−1052.
(35) Santos, L. M.; Machado, W. A.; França, M. D.; Borges, K. A.; Paniago, R. M.; Patrocinio, A. O. T.; Machado, A. E. H. Structural characterization of Ag-doped TiO2 with enhanced photocatalytic activity. *RSC Adv.* **2015**, *5*, 103752−103759.
(36) Chakhtouna, H.; Benzeid, H.; Zari, N.; Qaiss, A. e. k.; Bouhfid, R. Recent progress on Ag/TiO2 photocatalysts: photocatalytic and bactericidal behaviors. *Environ. Sci. Pollut. Res.* **2021**, *28*, 44638−44666.
(37) Gogoi, D.; Namdeo, A.; Golder, A. K.; Peela, N. R. Ag-doped TiO2 photocatalysts with effective charge transfer for highly efficient hydrogen production through water splitting. *Int. J. Hydrogen Energy* **2020**, *45*, 2729−2744.
(38) Varma, R. S.; Thorat, N.; Fernandes, R.; Kothari, D. C.; Patel, N.; Miotello, A. Dependence of photocatalysis on charge carrier separation in Ag-doped and decorated TiO2 nanocomposites. *Catal. Sci. Technol.* **2016**, *6*, 8428−8440.
(39) Zhao, Z.-J.; Hwang, S. H.; Jeon, S.; Hwang, B.; Jung, J.-Y.; Lee, J.; Park, S.-H.; Jeong, J.-H. Three-dimensional plasmonic Ag/TiO2 nanocomposite architectures on flexible substrates for visible-light photocatalytic activity. *Sci. Rep.* **2017**, *7*, No. 8915.
(40) Zhang, S.; Wang, L.; Liu, C.; Luo, J.; Crittenden, J.; Liu, X.; Cai, T.; Yuan, J.; Pei, Y.; Liu, Y. Photocatalytic wastewater purification with simultaneous hydrogen production using MoS2 QD-decorated hierarchical assembly of ZnIn2S4 on reduced graphene oxide photocatalyst. *Water Res.* **2017**, *121*, 11−19.
(41) Hippargi, G.; Anjankar, S.; Krupadam, R. J.; Rayalu, S. S. Simultaneous wastewater treatment and generation of blended fuel methane and hydrogen using Au-Pt/TiO2 photo-reforming catalytic material. *Fuel* **2021**, *291*, No. 120113.
(42) Jeon, T. H.; Koo, M. S.; Kim, H.; Choi, W. Dual-Functional Photocatalytic and Photoelectrocatalytic Systems for Energy- and Resource-Recovering Water Treatment. *ACS Catal.* **2018**, *8*, 11542−11563.
(43) Pitchaimuthu, S.; Sridharan, K.; Nagarajan, S.; Ananthraj, S.; Robertson, P.; Kuehnel, M. F.; Irabien, Á.; Maroto-Valer, M. Solar Hydrogen Fuel Generation from Wastewater—Beyond Photoelectrochemical Water Splitting: A Perspective. *Energies* **2022**, *15*, 7399.
(44) Liu, J.; An, T.; Li, G.; Bao, N.; Sheng, G.; Fu, J. Preparation and characterization of highly active mesoporous TiO2 photocatalysts by hydrothermal synthesis under weak acid conditions. *Microporous Mesoporous Mater.* **2009**, *124*, 197−203.
(45) Naik, B.; Desai, V.; Kowshik, M.; Prasad, V. S.; Fernando, G. F.; Ghosh, N. N. Synthesis of Ag/AgCl−mesoporous silica nanocomposites using a simple aqueous solution-based chemical method and a study of their antibacterial activity on E. coli. *Particuology* **2011**, *9*, 243−247.
(46) Yuan, J.; Chen, M.; Shi, J.; Shangguan, W. Preparations and photocatalytic hydrogen evolution of N-doped TiO2 from urea and titanium tetrachloride. *Int. J. Hydrogen Energy* **2006**, *31*, 1326−1331.
(47) Kresse, G.; Joubert, D. From ultrasoft pseudopotentials to the projector augmented-wave method. *Phys. Rev. B: Condens. Matter Mater. Phys.* **1999**, *59*, 1758−1775.
(48) Kresse, G.; Furthmüller, J. Efficiency of ab-initio total energy calculations for metals and semiconductors using a plane-wave basis set. *Comput. Mater. Sci.* **1996**, *6*, 15−50.
(49) Kresse, G.; Furthmüller, J. Efficient iterative schemes for ab initio total-energy calculations using a plane-wave basis set. *Phys. Rev. B: Condens. Matter Mater. Phys.* **1996**, *54*, 11169−11186.
(50) Perdew, J. P.; Chevary, J. A.; Vosko, S. H.; Jackson, K. A.; Pederson, M. R.; Singh, D. J.; Fiolhais, C. Atoms, molecules, solids, and surfaces: Applications of the generalized gradient approximation for exchange and correlation. *Phys. Rev. B: Condens. Matter Mater. Phys.* **1992**, *46*, 6671−6687.
(51) Perdew, J. P.; Burke, K.; Ernzerhof, M. Generalized Gradient Approximation Made Simple. *Phys. Rev. Lett.* **1996**, *77*, 3865−3868.
(52) Monkhorst, H. J.; Pack, J. D. Special points for Brillouin-zone integrations. *Phys. Rev. B: Condens. Matter Mater. Phys.* **1976**, *13*, 5188−5192.
(53) Dudarev, S. L.; Botton, G. A.; Savrasov, S. Y.; Humphreys, C. J.; Sutton, A. P. Electron-energy-loss spectra and the structural stability of nickel oxide: An LSDA+U study. *Phys. Rev. B: Condens. Matter Mater. Phys.* **1998**, *57*, 1505−1509.
(54) Kim, S.; Ji, S.; Kim, K. H.; Roh, S. H.; Cho, Y.; Lee, C.-L.; Lee, K.-S.; Choi, D.-G.; Choi, H.; Kim, J. K.; Park, J. H. Revisiting surface chemistry in TiO2: A critical role of ionic passivation for pH-independent and anti-corrosive photoelectrochemical water oxidation. *Chem. Eng. J.* **2021**, *407*, No. 126929.
(55) Sanjinés, R.; Tang, H.; Berger, H.; Gozzo, F.; Margaritondo, G.; Levy, F. Electronic structure of anatase TiO2 oxide. *J. Appl. Phys.* **1994**, *75*, 2945−2951.
(56) Bharti, B.; Kumar, S.; Lee, H.-N.; Kumar, R. Formation of oxygen vacancies and Ti 3+ state in TiO 2 thin film and enhanced optical properties by air plasma treatment. *Sci. Rep.* **2016**, *6*, No. 32355.
(57) Jaiswal, R.; Patel, N.; Kothari, D.; Miotello, A. Improved visible light photocatalytic activity of TiO2 co-doped with Vanadium and Nitrogen. *Appl. Catal., B* **2012**, *126*, 47−54.
(58) Wint, T. H. M.; Smith, M. F.; Chanlek, N.; Chen, F.; Oo, T. Z.; Songsiriritthigul, P. Physical origin of diminishing photocatalytic efficiency for recycled TiO2 nanotubes and Ag-loaded TiO2 nanotubes in organic aqueous solution. *Catalysts* **2020**, *10*, 737.
(59) Thiel, J.; Pakstis, L.; Buzby, S.; Raffi, M.; Ni, C.; Pochan, D. e. J.; Shah, S. I. Antibacterial properties of silver-doped titania. *Small* **2007**, *3*, 799−803.
(60) Wagner, C.; Riggs, W.; Davis, L.; Moulder, J.*Handbook of X-ray Photoelectron Spectroscopy*, Muilenberg, G. E., Ed.; Perkin-Elmer Corporation: Eden Prairie, Minnesota, 1979; p 38.
(61) Vasil'kov, A. Y.; Dovnar, R. I.; Smotryn, S. M.; Iaskevich, N. N.; Naumkin, A. V. Plasmon resonance of silver nanoparticles as a method of increasing their antibacterial action. *Antibiotics* **2018**, *7*, 80.
(62) Guan, W.; Ji, F.; Xie, Z.; Li, R.; Mei, N. Preparation and photocatalytic performance of nano-TiO2 codoped with iron III and lanthanum III. *J. Nanomater.* **2015**, *2015*, 1−13.
(63) Dal'Toé, A. T.; Colpani, G. L.; Padoin, N.; Fiori, M. A.; Soares, C. Lanthanum doped titania decorated with silver plasmonic nanoparticles with enhanced photocatalytic activity under UV−visible light. *Appl. Surf. Sci.* **2018**, *441*, 1057−1071.
(64) Guo, J.; Cai, X.; Li, Y.; Zhai, R.; Zhou, S.; Na, P. The preparation and characterization of a three-dimensional titanium dioxide nanostructure with high surface hydroxyl group density and high performance in water treatment. *Chem. Eng. J.* **2013**, *221*, 342−352.
(65) Wang, B.; Zhang, G.; Sun, Z.; Zheng, S.; Frost, R. L. A comparative study about the influence of metal ions (Ce, La and V) doping on the solar-light-induced photodegradation toward rhodamine B. *J. Environ. Chem. Eng.* **2015**, *3*, 1444−1451.
(66) Lei, X.; Chen, C.; Li, X.; Xue, X.; Yang, H. Characterization and photocatalytic performance of La and C co-doped anatase TiO2 for photocatalytic reduction of Cr (VI). *Sep. Purif. Technol.* **2016**, *161*, 8−15.
(67) Sing, K. S. W. Reporting physisorption data for gas/solid systems with special reference to the determination of surface area and porosity (Recommendations 1984). *Pure Appl. Chem.* **1985**, *57*, 603−619.
(68) Raj, K. J. S.; Viswanathan, B. Effect of surface area, pore volume and particle size of P25 titania on the phase transformation of anatase to rutile. *Indian J. Chem., Sect. A: Inorg., Phys., Theor. Anal.* **2009**, *48*, 1378−1382.
(69) Deiana, C.; Fois, E.; Coluccia, S.; Martra, G. Surface Structure of TiO2 P25 Nanoparticles: Infrared Study of Hydroxy Groups on Coordinative Defect Sites. *J. Phys. Chem. C* **2010**, *114*, 21531−21538.

https://doi.org/10.1021/acsomega.2c06657
ACS Omega 2023, 8, 1249−1261

(70) Bendahou, K.; Cherif, L.; Siffert, S.; Tidahy, H.; Benaissa, H.; Aboukais, A. The effect of the use of lanthanum-doped mesoporous SBA-15 on the performance of Pt/SBA-15 and Pd/SBA-15 catalysts for total oxidation of toluene. *Appl. Catal., A* **2008**, *351*, 82−87.
(71) Dai, K.; Peng, T.; Chen, H.; Liu, J.; Zan, L. Photocatalytic degradation of commercial phoxim over La-doped TiO2 nanoparticles in aqueous suspension. *Environ. Sci. Technol.* **2009**, *43*, 1540−1545.
(72) Shi, Z.-l.; Lai, H.; Yao, S.-h.; Wang, S.-f. Preparation, characterization and photocatalytic activity of lanthanum doped mesoporous titanium dioxide. *Chin. J. Chem. Phys.* **2012**, *25*, 96.
(73) Wang, J.; Tafen, D. N.; Lewis, J. P.; Hong, Z.; Manivannan, A.; Zhi, M.; Li, M.; Wu, N. Origin of photocatalytic activity of nitrogen-doped TiO2 nanobelts. *J. Am. Chem. Soc.* **2009**, *131*, 12290−12297.
(74) Kumar, M. P.; Jagannathan, R.; Ravichandran, S. Photo-electrochemical system for unassisted high-efficiency water-splitting reactions using N-doped TiO2 nanotubes. *Energy Fuels* **2020**, *34*, 9030−9036.
(75) Asahi, R.; Morikawa, T.; Ohwaki, T.; Aoki, K.; Taga, Y. Visible-light photocatalysis in nitrogen-doped titanium oxides. *Science* **2001**, *293*, 269−271.
(76) Gomes, J.; Lincho, J.; Domingues, E.; Quinta-Ferreira, R. M.; Martins, R. C. N−TiO2 photocatalysts: A review of their characteristics and capacity for emerging contaminants removal. *Water* **2019**, *11*, 373.
(77) Zaleska, A. Doped-TiO2: a review. *Recent Pat. Eng.* **2008**, *2*, 157−164.
(78) Matthews, R. W.; Abdullah, M.; Low, G. K. C. Photocatalytic oxidation for total organic carbon analysis. *Anal. Chim. Acta* **1990**, *233*, 171−179.
(79) Liu, Y.; Xie, L.; Li, Y.; Qu, J.; Zheng, J.; Li, X. Photocatalytic Hydrogen Generation Over Lanthanum Doped TiO2 Under UV Light Irradiation. *J. Nanosci. Nanotechnol.* **2009**, *9*, 1514−1517.
(80) Zhao, Y.; Wang, W.; He, L. The effects of Co/N dopants on the electronic, redox potential, optical, and photocatalytic water-splitting properties of TiO2: First principles calculations. *Chem. Phys. Lett.* **2017**, *685*, 108−113.
(81) Eidsvåg, H.; Bentouba, S.; Vajeeston, P.; Yohi, S.; Velauthapillai, D. TiO2 as a Photocatalyst for Water Splitting—An Experimental and Theoretical Review. *Molecules* **2021**, *26*, 1687.
(82) Shwetharani, R.; Sakar, M.; Chandan, H.; Balakrishna, R. G. Observation of simultaneous photocatalytic degradation and hydrogen evolution on the lanthanum modified TiO2 nanostructures. *Mater. Lett.* **2018**, *218*, 262−265.
(83) Choi, H.; Khan, S.; Choi, J.; Dinh, D. T. T.; Lee, S. Y.; Paik, U.; Cho, S.-H.; Kim, S. Synergetic control of band gap and structural transformation for optimizing TiO2 photocatalysts. *Appl. Catal., B* **2017**, *210*, 513−521.
(84) Singh, B.; Mehta, B. R. Relationship between nature of metal-oxide contacts and resistive switching properties of copper oxide thin film based devices. *Thin Solid Films* **2014**, *569*, 35−43.
(85) Grätzel, M. Photoelectrochemical cells. *Nature* **2001**, *414*, 338−344.
(86) Malik, A. S.; Liu, T.; Dupuis, M.; Li, R.; Li, C. Water Oxidation on TiO2: A Comparative DFT Study of 1e−, 2e−, and 4e− Processes on Rutile, Anatase, and Brookite. *J. Phys. Chem. C* **2020**, *124*, 8094−8100.
(87) Valdés, Á.; Qu, Z. W.; Kroes, G. J.; Rossmeisl, J.; Nørskov, J. K. Oxidation and Photo-Oxidation of Water on TiO2 Surface. *J. Phys. Chem. C* **2008**, *112*, 9872−9879.
(88) Jallouli, N.; Elghniji, K.; Trabelsi, H.; Ksibi, M. Photocatalytic degradation of paracetamol on TiO2 nanoparticles and TiO2/cellulosic fiber under UV and sunlight irradiation. *Arabian J. Chem.* **2017**, *10*, S3640−S3645.
(89) López Zavala, M. Á.; Jaber Lara, C. R. Degradation of Paracetamol and Its Oxidation Products in Surface Water by Electrochemical Oxidation. *Environ. Eng. Sci.* **2018**, *35*, 1248−1254.
(90) Moctezuma, E.; Leyva, E.; Aguilar, C. A.; Luna, R. A.; Montalvo, C. Photocatalytic degradation of paracetamol: Intermediates and total reaction mechanism. *J. Hazard. Mater.* **2012**, *243*, 130−138.
(91) Xiong, Z.; Ma, J.; Ng, W. J.; Waite, T. D.; Zhao, X. Silver-modified mesoporous TiO2 photocatalyst for water purification. *Water Res.* **2011**, *45*, 2095−2103.

https://doi.org/10.1021/acsomega.2c06657
ACS Omega 2023, 8, 1249−1261